Strength of porous oxide microspheres: the role of internal porosity and defects

Paul Parant, Sébastien Picart, Pierre Lhuissier, Christophe L. Martin

Strength of porous oxide microspheres: the role of internal porosity and defects

Paul Parant[a,b], Sébastien Picart[a,*], Pierre Lhuissier[b], Christophe L. Martin[b,*]

[a] *CEA, Nuclear Energy Division, Research Department of Mining and Fuel Recycling ProCesses, F-30207 Bagnols-sur-Cèze, France*

[b] *Univ. Grenoble Alpes, CNRS, SIMAP, F-38000 Grenoble, France*

Abstract

Ceramic oxide green pellets for nuclear fuel or targets are manufactured by powder processes producing detrimental fines. Porous brittle microspheres offer an interesting alternative, providing that their fracture behaviour is well controlled during pressing. Here we investigate, using experimental characterization and numerical simulations, the effect of internal defects on the strength of porous microspheres. We show that although the residual porosity is the main parameter affecting their strength, the shape and location of defects also play a role. Real defects characterized by X-ray tomography are reproduced with discrete element simulations, providing new insights on their fracture behaviour. We also investigate the departure from monosized microspheres by simulating the fracture behaviour of two microspheres of different sizes, and show that it is the minimum radius that allows for a consistent strength normalization. This study offers a method for anticipating agglomerate strength that can be generalized for any ceramic systems.

Keywords: porous microsphere, defect, Discrete Element Method, X-ray tomography, pressing

1. Introduction

Ceramic nuclear fuel pellets are typically produced by powder metallurgy processes with numerous grinding and milling steps that generate very fine particles [1, 2]. This is an issue for nuclear fuel fabrication as these fines are highly contaminating, irradiating and more difficult to handle. Thus, the development of a dustless process with brittle granulated precursors, obtained by the "Weak Acid Resin" process or sol-gel processes [3, 4, 5, 6, 7], is of interest for the nuclear industry. More generally, whatever the material of particles, working with much coarser particles facilitates the flow and the filling of pressing dies in powder metallurgy [8, 9, 10].

The control of the shaping of these ceramic granulated precursors by uni-axial pressing to obtain uniform pellets is essential. Prior to sintering, the green microstructure should be as homogeneous as possible to ensure defect-free pellets. During pressing, the brittle porous microspheres deform and break to decrease the overall porosity of the green pellet.

*Corresponding author. Email: christophe.martin@grenoble-inp.fr, sebastien.picart@cea.fr

The mutual interaction of these porous microspheres under uni-axial pressing dictates the uniformity of pellets. However, it is not sufficient to study only the elastic interaction of those granulated precursors. The full mechanical history, starting with intact spheres interacting through their contacts followed by large chunks of fractured microspheres indenting each other must be investigated. Indeed, we have shown experimentally and numerically that multiple discrete fracture processes occur at the scale of micronic aggregates (assumed unbreakable for lanthanide oxides) [11]. The strength of ceramic precursors depend on several factors: their internal porosity, their composition and the calcination temperature. Furthermore, macroscopic microstructural defects have been identified and indicate the presence of macro-porosities in the internal structure of microspheres. These defects that are inherent to any industrial process will inevitably impact the microsphere strength. In our preceding study the brittle granulate was modelled by a sub-milimetric microsphere (regular sphericity) consisting of a homogeneous assembly of micronic aggregates, thus neglecting any internal defect [11].

The Discrete Element Method (DEM) is a powerful tool for the numerical simulation of these brittle microspheres that are constituted by a discrete assembly of aggregates. In DEM, the inherently discrete nature of porous microspheres can be taken into account in a natural manner. The use of a simple fracture criterion at the junction between aggregates allows for the simulation of the breaking of micropspheres. The handling of the multiple topological modifications that come with microsphere fracture is much easier with DEM than with FEM (Finite Element Method) simulations. There is no need to predefine the location of cracks as in FEM [12]. DEM can also naturally account for the frictional contacts between the newly created surfaces and thus provides the required ingredients for the explicit modeling of multiple microspheres or granulates interacting with each other.

Using DEM simulations coupled with experimental characterization, the purpose of this paper is therefore to study the influence of defects and microstructure on the mechanical strength of porous microspheres and to relate their tensile strength to their porosity characteristics. The interest of such a study goes beyond lanthanide oxides, since porous agglomerates are ubiquitous in ceramic processes. Defect modeling with DEM requires accurate three-dimensional defect characterization that only X-ray nano-tomography can provide. This is why we attempt here to use X-ray nano-tomography images as inputs for DEM simulations. This strong coupling with experimental characterization has the advantage of simulating the exact shape of defects and capturing the deviation from sphericity of the microsphere.

2. Materials and methods

2.1. Microsphere synthesis

The lanthanide oxide precursors are synthesized via the Weak Acid Resin (WAR) process, which uses ion exchange resin beads to fix metal cations and act as an organic spherical template and, after heat treatment, produce the oxide microspheres. More details on the synthesis of oxide microspheres can be found in previous studies [8, 11]. Here, mixed cerium-gadolinium oxide microspheres were produced with different lanthanide ratios in order to surrogate heavy metallic oxide compounds with fluorine structure [11]. In this respect, the proportions of gadolinium involved in oxides should not exceed 30-40% [13, 14] and it was therefore decided to work on compounds with the following Ce/Gd ratios : 90/10; 80/20; 70/30 and 60/40. Another means of controlling microsphere's density is to use a

Oxides	Furnace	Mean diameter (μm $\pm$10)	Relative density (%TD $\pm$2)	Structure
CeO_2 [11]	Muffle	490	17.0	Fluorine
$Ce_{0.9}Gd_{0.1}$	Muffle	460	21.6	Fluorine
$Ce_{0.8}Gd_{0.2}$	Muffle	430	22.4	Fluorine
$Ce_{0.7}Gd_{0.3}$	Muffle	440	24.0	Fluorine
$Ce_{0.6}Gd_{0.4}$	Muffle	440	25.5	Fluorine
Gd_2O_3 [11]	Muffle	380	37.0	Cubic
Gd_2O_3	Tubular	310	55.0	Cubic

Table 1: Physico-chemical properties of cerium-gadolinium mixed oxides. Where $Ce_{0.9}Gd_{0.1}$, $Ce_{0.8}Gd_{0.2}$, $Ce_{0.7}Gd_{0.3}$, $Ce_{0.6}Gd_{0.4}$ stand for $(Ce_{0.9}Gd_{0.1})O_{1.95\pm\delta}$, $(Ce_{0.8}Gd_{0.2})O_{1.9\pm\delta}$, $(Ce_{0.7}Gd_{0.3})O_{1.85\pm\delta}$ and $(Ce_{0.6}Gd_{0.4})O_{1.8\pm\delta}$, respectively.

different furnace for calcination. In the previous study, the furnace used for the calcination of gadolinium microspheres is a static air muffle furnace. In this study, gadolinium microspheres are calcined in a tubular furnace in which a reconstituted air flow is provided during the calcination process. The physico-chemical properties of gadolinium oxides and mixed oxides are summarized in Table 1. By way of comparison, the microspheres made of simple oxides CeO_2 and Gd_2O_3 calcined in a muffle furnace have, under the same operating conditions (temperature, initial resins), a relative density (ρ) equal to 17 %TD and 37 %TD [11], respectively.

The density of the oxide microspheres increases as the gadolinium content increases while their diameters tend to decrease. The changes in apparent density of mixed microspheres as a function of their composition are presented in Table 1 and compared to the density of simple oxides CeO_2 and Gd_2O_3 [11]. The increase in density with gadolinium content seems to be related to the release of heat during calcination. The energy emitted during the degradation of the carbon skeleton has an influence on the properties of the oxide precursors such as their density, for example. This is because the higher the energy emitted, the greater the porosity in the oxide [15]. In addition, the calcination of gadolinium microspheres in a tubular furnace leads to a densification of the microstructure through better gas evacuation during calcination and allows a density of 55%TD to be achieved, which will result in differences in mechanical behaviour.

2.2. X-ray Tomography

The internal microstructure of the microspheres was studied by X-ray adsorption tomography. Using the collected data, a digital image is calculated and reconstructed in gray-scale corresponding to the local attenuation factor. X-ray tomography was performed on the SIMaP laboratory nanotomograph (RX Solutions) equipped with a nanofocus transmission source (Hamamatsu) and a cooled QuadRO CDD (Princeton Instruments) using a CsI scintillator on a 1:1 taper. Two spheres have been imaged. For the first one, 1600 projections of 8s at 60kV beam voltage have been used for a 3D reconstruction on a 200nm voxel size grid. For the second sphere, 800 projections of 6s exposure time at 90kV beam voltage have been used for a 3D reconstruction on a 300nm voxel size grid. In both cases, a 0.25mm thick aluminum filter has been used to reduce beam hardening. Source spot size, detector modulation transfer function

and chosen magnification led to a submicron resolution. This resolution is sufficient to image a defect in detail.

2.3. Experimental characterization of mechanical properties

The mechanical properties of the microspheres were characterized by recording the crushing of a microsphere using a DEBEN micropress (Mini tensile tester 200 N) equipped with a 5 N or 200 N load cell. Crushing is achieved by controlling the movement of two compression modules moving at a constant and slow enough speed (0.1 mm/min) to avoid inertial phenomena. Crushing tests were performed in-situ into a Scanning Electron Microscope (Zeiss, SEM FEG Supra 55) to monitor the microsphere deformation and its evolution during crushing while recording the force value. These in-situ SEM observations allow local damage and cracks to be followed.

2.4. Discrete Element model

The Discrete Element Method (DEM) is used to simulate the crushing of oxide microspheres. The porous microsphere is modelled as an assembly of discrete spherical particles (radius r) that interact with each other through their contacts. A more detailed description is given in the original model paper [16] and its application for porous microspheres crushing [11] and for compaction [17, 18]. Here, we only summarize the main concepts of the DEM model. In short, the total force acting on a given particle is computed from contact forces of neighbouring particles. Here, contacts are stiff bonds between particles that have formed during calcination. The unbreakable unit particle is a sphere and models an aggregate (diameter: 2 μ m). Aggregates are linked with their contacting neighbours by breakable bonds. Before breakage, a bond behaves elastically in tension, compression, and shear with stiffness that are essentially characterized by the bond radius (radius a) and and by the Young's modulus of the particles (E) [19, 20]. The size of bonds is dictated by the calcination process. Rotation of particles is an important aspect of the model and resisting moments that oppose relative rotations between two bonded particles are fully accounted for [21].

A fracture criterion completes the model. The maximum tensile and shear stresses that act at the periphery of the beam can be evaluated by approximating the bond to a cylindrical beam [21]. Together with the specification of a bond strength (σ_b), the knowledge of these tensile and shear stresses leads to a simple fracture criterion that has been quantitatively validated on Al_2O_3, NiO and YSZ partially sintered ceramics [22]. Note that for simplicity, the same strength is used in tension and shear. Once fractured, a bond does not transmit any tensile stress but it may still transmit a compressive force (with the same normal stiffness as the unbroken bond) or a shear force (due to friction with μ=0.5).

3. Crushing of porous oxide microspheres

3.1. SEM and X-ray tomography observations

A defect was observed on mixed microspheres $(Ce_{0.8}Gd_{0.2})O_{2\pm\delta}$ by SEM observations on broken microspheres as shown in Fig. 1. The central hole appears ellipsoidal in shape with a length corresponding to 30% of the diameter of the microsphere and a width of just 6% of the diameter. The total volume occupied by the central defect therefore appears small compared to the total volume of the microsphere.

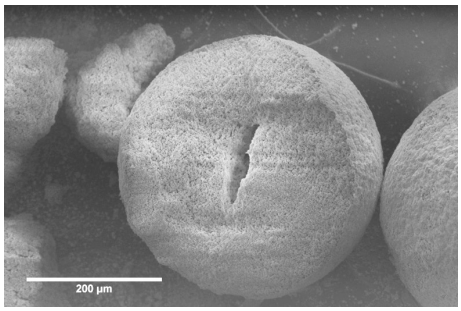

Figure 1: SEM images of a $(Ce_{0.8}Gd_{0.2})O_{2\pm\delta}$ microsphere calcined at 800 ℃.

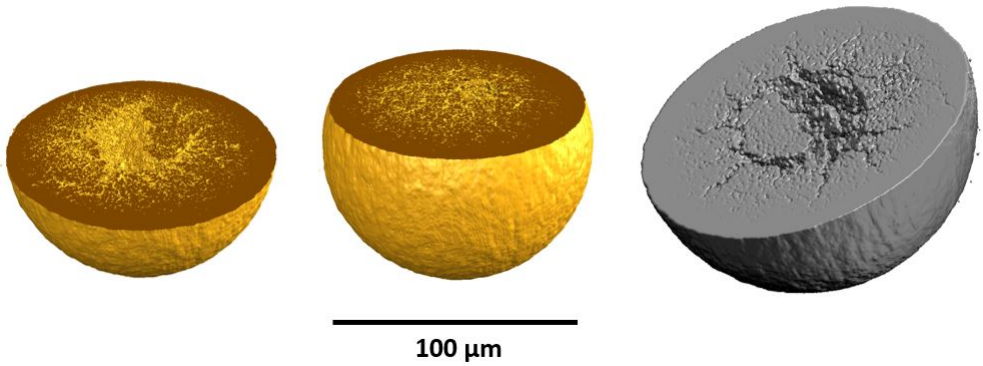

Figure 2: X-ray tomography images of a Gd_2O_3 microsphere calcined at 800 ℃ in a muffle furnace. Pixel size=200 nm.

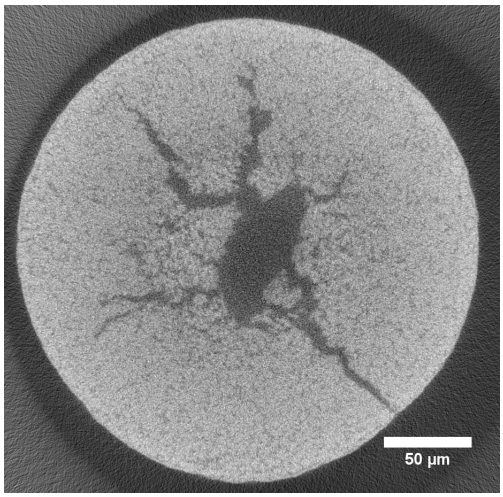

Figure 3: X-ray tomography observation of a Gd_2O_3 microsphere calcined in a tubular furnace at 800 ℃. Pixel size=300 nm

The presence of a central cavity is also observed on X-ray tomography images. Remy [23] showed for CeO_2 microspheres that the presence of these defects is inherent to the preparation of the resin and was preserved during the transformation into oxide microspheres. This central defect was observed by X-ray tomography (Fig. 2) on the gadolinium microsphere calcined at 800 ℃ as discussed in a previous study [11]. Fig. 3 shows that the defect located in the center of the microsphere exhibits cracks starting from this defect and propagating towards the surface of the microsphere. The geometry of this defect cannot be generalized to all gadolinium microspheres but it seems intuitive that those cracks should have an impact on the mechanical properties of microspheres. DEM simulations based on this X-ray tomography image will investigate this issue (see section 4.2).

3.2. Mechanical properties

Modulation of porosity in oxide microspheres thanks to the gadolinium content (see table 1) allows to modulate the properties of the oxides as shown in Fig. 4. Those properties have an effect on mechanical properties and especially the strength of the microspheres which increases with the gadolinium content from 14 mN for microspheres of $(Ce_{0.9}Gd_{0.1})O_{1.95\pm\delta}$ to 90 mN for microspheres of $(Ce_{0.6}Gd_{0.4})O_{1.8\pm\delta}$ obtained after calcination at 800 ℃. Fig. 4 shows the evolution of the crushing force of mixed oxide microspheres calcined at 800 ℃ as a function of their density. The so-called simple cerium and gadolinium oxide microspheres (respectively CeO_2 and Gd_2O_3 [11]) are also shown on the graph. It can be seen that the crushing load tend to increase with density. Microspheres with low densities, i. e. low gadolinium content, exhibit very low crushing load. When the density starts to increase, the crushing load increases sharply. This clear dependence of the breaking force value on density was observed by Ferreira et al. [24] during the crushing of uranium oxide microspheres obtained by the sol-gel route.

Since microspheres exhibit different diameters depending on their content (see Table 1), it is more meaningful to compare fracture stresses of the different synthesized microspheres, providing a normalizing surface can be found. The following general equation is used for the

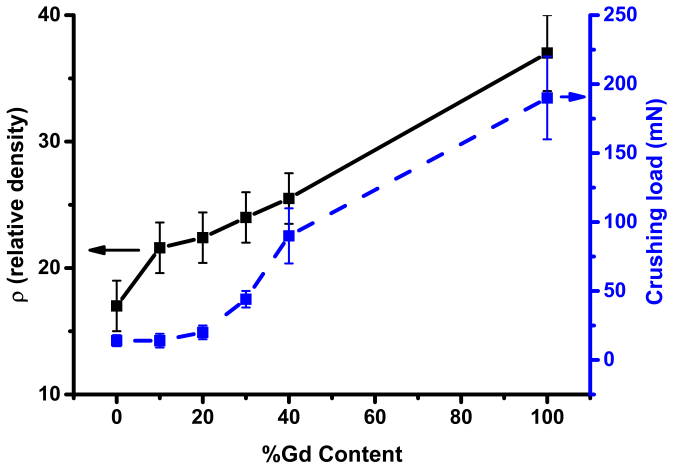

Figure 4: Evolution of the relative density and the crushing load of mixed oxide microspheres as a function of gadolinium content.

microsphere strength:

$$\sigma_{max} = \kappa \frac{F_{max}}{\pi R^2} \tag{1}$$

where the value of κ is debated [25, 26, 27, 28] but in any case close to unity if fracture occurs by tension inside the sphere. Fig. 5 shows on a log-log plot the evolution of the maximum stress, σ_{max}, as a function of the density of microspheres (different calcination temperatures, compositions or furnaces) for $\kappa = 0.7$ [25]. The evolution of the fracture stress shows that it is essentially guided by the density of the oxide microsphere following approximately a power law:

$$\sigma_{max} = \sigma_0 . \rho^n \tag{2}$$

with σ_0=79 MPa, $n = 4.1$. This simple power law erases many of the specific details of the microspheres inherent to each precursor and each mode of synthesis and calcination. However, it makes it possible to anticipate an approximate value of the fracture stress as a function of relative density, which remains the first order parameter for the fracture properties of microspheres.

4. DEM simulations of the crushing of oxide microsphere with defects

The DEM simulation of the crushing of microspheres with defect is performed using material parameters that characterize the mechanical properties of Gd_2O_3 aggregates and their mutual interactions (table 2). These properties are the bond radius (a), the Young's modulus of the aggregate (E) and the bond strength (σ_b). They are identical to those used in a previous paper and are fitted to match force versus displacement curves obtained experimentally [11]. In particular, we have shown that the fitting of these three parameters allowed for a very good match of the non-linear force versus strain curve. Table 2 summarizes these parameters. Note that the two platens that serve to crush the microspheres are much stiffer and harder than the microspheres (Young's modulus 300 GPa and no plastic yielding).

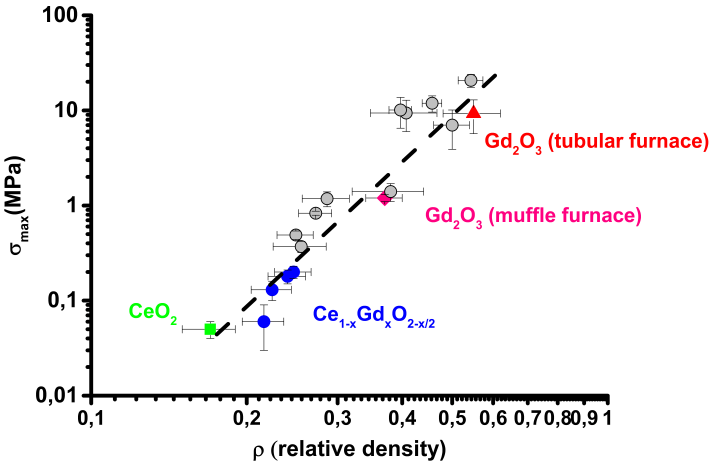

Figure 5: Evolution of tensile strengths of all synthesized oxide microspheres as a function of relative density.

particle number	particle diameter	bond radius	Young's modulus	bond strength
$\simeq$380 000	$r = 1\mu$m	$a = 0.2 \times r$	$E = 20.0$ GPa	$\sigma_b = 0.25$ GPa

Table 2: Material parameters of the DEM model for Gd_2O_3 porous aggregates [11]. r is the radius of the unbreakable aggregate.

In this section, we investigate the impact of an internal defect on the fracture behavior of a microsphere.

In order to have a logical comparison between the various defects tested, we started from the exact same defect-free microsphere (diameter $d = 170\mu$m) . This microsphere was generated numerically from the X-ray tomography image (Fig. 2) with the internal defect removed. Fig. 6 shows the 6 microspheres with defects that were simulated for strength with DEM, starting from the defect free microsphere. White particles in these simulated microspheres are simply removed to form a controlled defect (except for the last defect which mimics the X-ray tomography image, Fig. 2f). Note that microspheres a, b and c have the same number of aggregates removed. In other words, the defects in these three microspheres have the same volume (the relative defect volume is 1.4% of the total volume). Similarly, the defects in microspheres d, e and f have the same volume (4.6% of the total volume). Although defects depicted in Fig. 6b and c have the same volume fraction, their impact on mechanical strength may be quite different as defect in Fig. 6c is close to the surface. Such a condition is typical of the defect observed by nano-tomography in Fig. 3.

In accordance with earlier investigations on the crushing of brittle spheres [25, 26], we have observed that the maximum compressive force (defined as the strength force or crushing load) scales fairly well with the square of the diameter ($2R$) of the microsphere [11]. Thus the strength of a given microsphere may be considered size independent (providing it contains a sufficient number of aggregates) as suggested by Eq. (1).

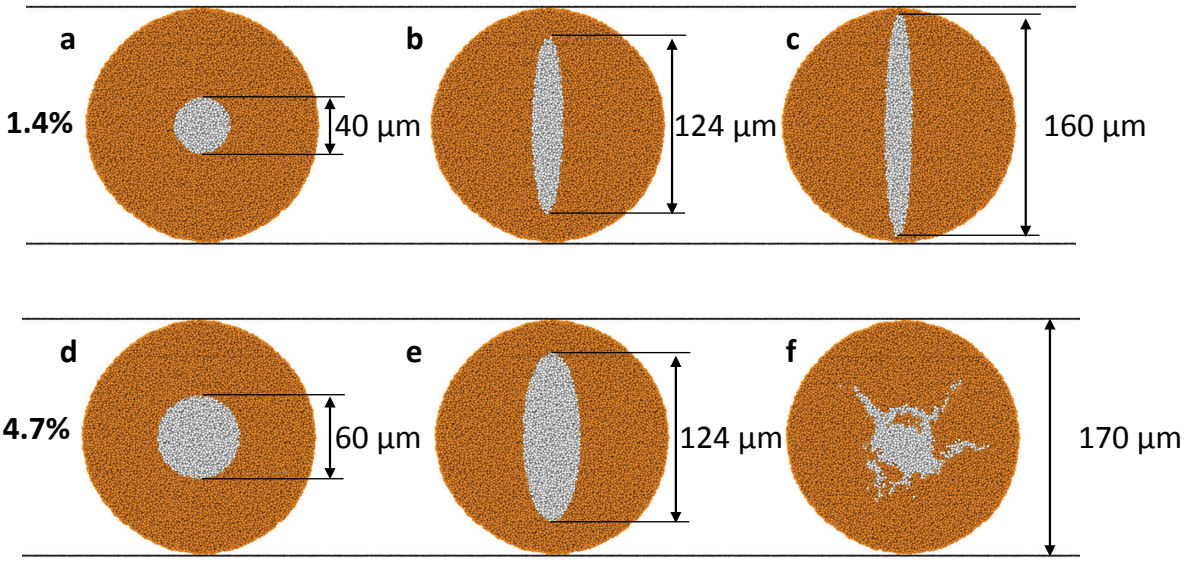

Figure 6: DEM simulated microspheres (diameter 170 μm) with defects a) spherical, b) ellipsoidal, c) ellipsoidal close to the microsphere surface, d) spherical, e) ellipsoidal, and f) real defect from X-ray tomography image (Fig. 2). White particles are removed to create the central defect. The relative volume of the defect is given as a percentage for small defects (a,b, c) and large defects (d, e, f).

4.1. Idealized defects

Fig. 7 shows the result of the DEM simulation crushing tests on the idealized defects depicted in Fig. 6. Microspheres with a spherical defect exhibit crushing curves that are almost identical to the flawless microsphere. In contrast, defects with an elliptic geometry (with the large axis of the ellipse along the crushing axis) clearly affect the crushing behavior. For such defects, the strength of the microsphere is decreased and the force evolution with axial strain is modified with indications of earlier damage. The orientation of the defect versus the crushing axis also has a clear influence. Tilting the large elliptic defect by 90° (normal to the crushing axis) makes the defect much less detrimental to the strength of the microsphere. These results can be understood by investigating how damage spreads into the microsphere.

The spread of damage in the microsphere is exemplified in Fig. 8 for the ellipsoidal defect (Fig. 6b). We have observed that it is typical of simulation results of the crushing of microspheres (whatever the shape of the initial defect). Fig. 8 shows that damage starts at the vicinity of the platens in the form of a cone. A high stress concentration develops under the small area of contact between the platens thus shading the particle from the detrimental effect of the internal defect.

At 2.7% strain (around the force maximum in Fig. 7), this cone-shaped zone has been driven into the microsphere and an approximately planar crack develops from one of the platens (here the top platen) to reach the full diameter of the microsphere. In this example, a single meridional macrocrack develops (note also the initiation of a second crack which does not spread further for $\varepsilon \leq 4\%$). However, we have observed both experimentally and in DEM simulations that more cracks (two or three) may also develop. The final crack pattern depends predominantly on the energy input or equivalently on the crushing velocity

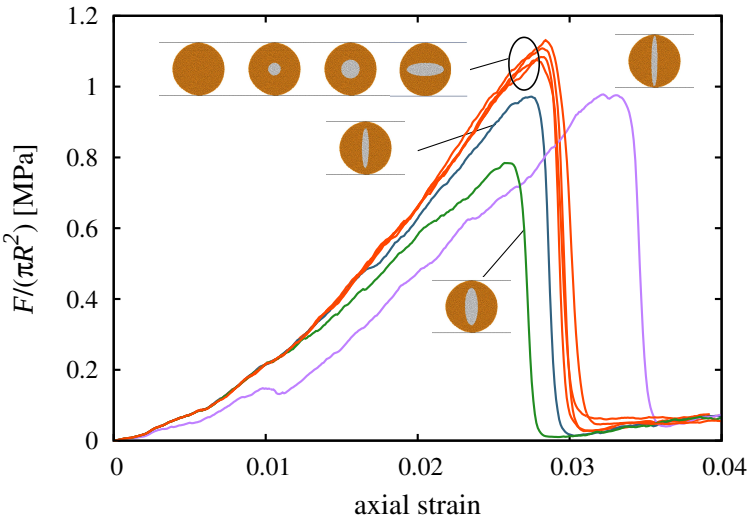

Figure 7: Axial force divided by the particle cross-sectional area, $F/\pi R^2$, versus axial strain for 7 microspheres crushed in between platens. Insets refer to the idealized defects depicted in Fig. 6.

as classically demonstrated by investigations related to comminution [29]. Here, since the crushing tests are carried out in quasi-static conditions (small velocities), they belong to the regime where damage spreads first followed by fragmentation in a small number of large fragments.

In any case, Fig. 8 clearly indicates that it is the zone close to the contact that dictates first the spreading of damage and then the macrocrack initiation. Thus, it explains the various groups of curves in Fig. 7, where microsphere with defects that do not spread close to the contact zone have nearly no impact, while defects that develop close to the contact impact the microsphere strength.

This result shows that porous microspheres do not fall into the standard theoretical framework of elastic brittle dense spheres under static compression. In this theoretical framework, a local maximum tensile stress concentration, which triggers fracture, arises at approximately $r/R = 0.8$ under the contact load [26]. This is clearly not the case for the microspheres investigated here, which exhibit damage just under the contact area. This damage occurs by a combination of shear and compressive stresses.

The DEM simulations (and the experiments as reported in [11]) used platens that are much harder and stiffer than the porous microspheres. Thus, the damage spreading shown in Fig. 8 may result predominantly from the high stress concentration just below the platens and could be artificially dominated by the mechanical contrast between the stiff platen and the relatively soft microsphere [27, 28]. To ensure that this was not the case, we have carried out simulations with two identical microspheres contacting each other and using periodic conditions on the sides. Under such conditions, no contact with platens exist since microspheres only contact each other. We observed that damage and fracture under those conditions (that are closer to the actual compaction into a die) are basically identical to those observed when crushing microspheres between two platens.

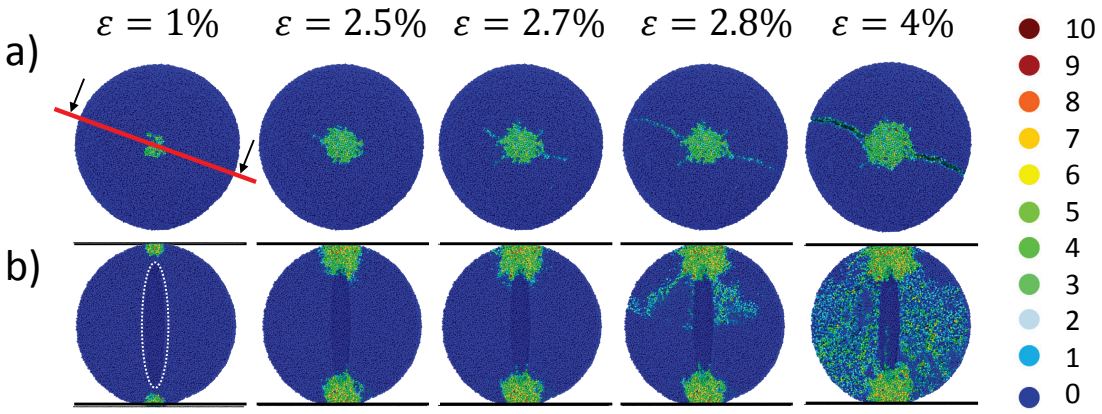

Figure 8: Damage evolution in a microsphere with a ellipsoidal defect (Fig. 6b) during a crushing test at increasing strain. The defect is highlighted in white. a) top view. b) slices (the cutting plane is indicated by the red arrows on the top view). Colours indicate the number of broken bonds per particle.

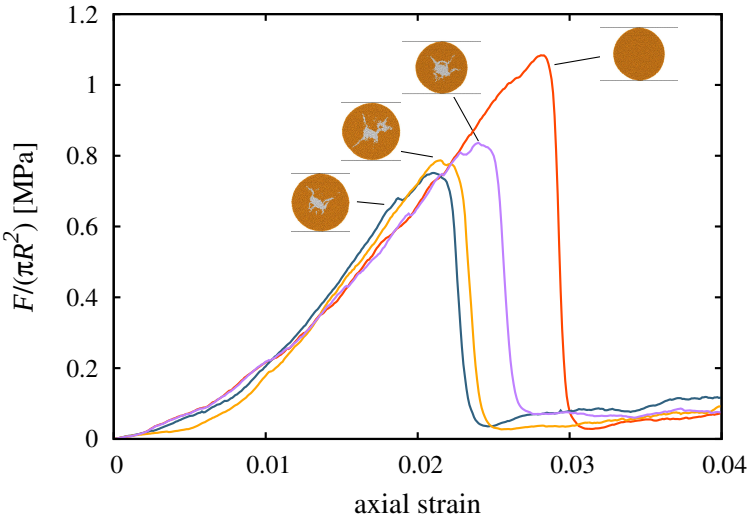

Figure 9: Axial force divided by the particle cross-sectional area, $F/\pi R^2$, versus axial strain for a microsphere without any defect and a microsphere with a defect from X-ray tomography image crushed in 3 different directions.

4.2. Realistic defect from X-ray tomography image

The X-ray tomography grayscale image (Fig. 2) is binarized in order to obtain a black (void) and white (material) image. From the binary image, the volume of the observed central defect is extracted and coupled with a simulation box containing spherical aggregates (2 μm in diameter, Fig. 6f). Particles in this defect-free aggregate are removed when they intersect a black voxel. The microstructure observed in tomography can thus be represented in DEM almost identically. The density of this simulated microsphere, taking into account the central defect, is 0.60.

Figure 9 compares the force versus deformation curves for a microsphere without any defect (ρ=0.64), for the same microsphere with a central defect characterized from X-ray tomography as described above (ρ=0.6) and loaded under three different directions.

The three curves characterizing the microsphere with the X-ray tomograph show some dispersion but lead to a similar strength to the one given by ideal ellipsoid defects of the same relative size (defect depicted in Fig. 6e). Again, this can be explained by the fact that the realistic defect captured by X-ray tomography exhibits branches which span close to the contacts.

5. Crushing of two size microspheres

In the preceding section, the effect of departing from a defect-free microsphere was studied. Another practical condition of importance is the case of a non-monomodal packing of microspheres. In that case, it is interesting to anticipate which microspheres are most likely to fracture first. We have thus simulated by DEM the mutual crushing of two spheres of different sizes. The size ratio was set to 1.4. We carried out simulations with two microspheres with elliptic defects (with their long axis aligned with the loading direction) that have the same relative size (i.e. the defects have the same volume fraction in the two microspheres). As reference, we also tested two defect-free microspheres.

Fig. 10a shows the crushing of the two microspheres with elliptic defects after 4% total strain. Although the large sphere exhibits traces of damage at the junction with the small sphere (and at the contact with the lateral platen), it is the small sphere that opens up into three large fragments. Note that we observed either two (see Fig. 8) , three (Fig. 10a) or four large fragments. We observed that the test with defect-free microspheres also leads to the fracture of the smallest microsphere. These simulation results are consistent with SEM observations of crushed pairs of gadolinium oxide microspheres with the same size ratio (Fig. 10b), where the smallest microsphere consistently broke first (see the video in the supplementary information).

The breaking of the smallest sphere is not fully intuitive but may be understood by considering Eq. (1). This equation simply states that the strength of a microsphere scales with the inverse of the square of the microsphere size, irrespective of the fracture mechanism (surface or volume defect in tension, or as in our case contact point failure). Force equilibrium between the two microspheres thus imposes that the characteristic stress that triggers fracture is attained first by the smallest microsphere.

Fig. 10c compares the stress evolution of the crushing curves for the test using two microspheres of different or equal sizes and for the test using a single microsphere. All tests are carried out with elliptic defects. Here we have used the minimum radius R_{min} to

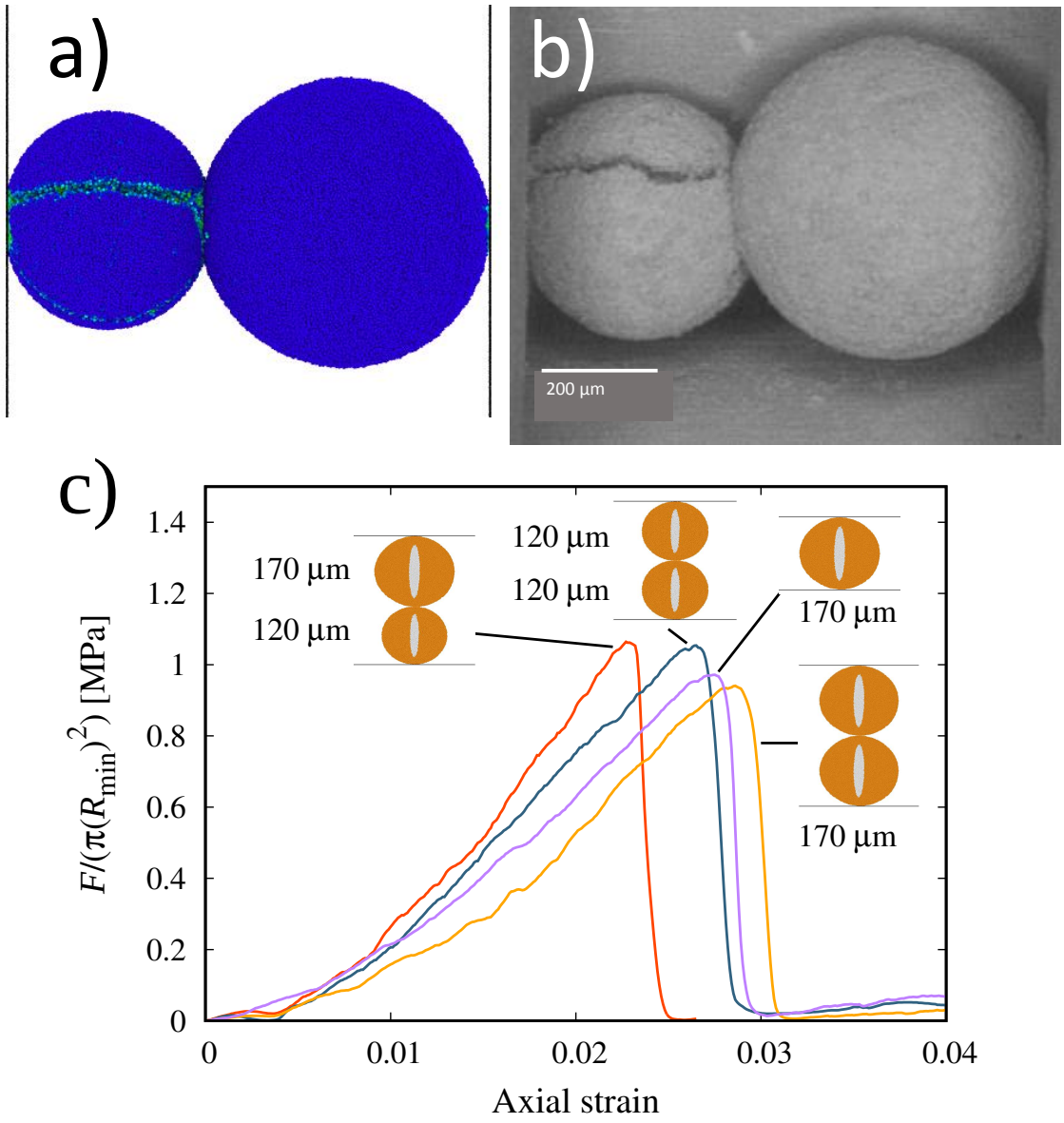

Figure 10: Mutual crushing of two microspheres of different sizes. a) DEM simulation. b) SEM in-situ crushing test of gadolinium oxide microsphere (calcined at 800 ℃). c) Force divided by the minimum particle cross-sectional area versus strain.

normalize the axial force F by the particle cross-sectional area. Fig. 10c shows that the four test curves approximately lead to the same maximum strength. The use of the minimum radius for anticipating forces when crushing non monomodal microspheres is consistent with our experimental observations (Fig. 10b) and with Eq. (1).

6. Conclusion

Granulated precursors have attracted a renewed interest for nuclear ceramic pellet fabrication as they allow for a drastic limitation of powder dissemination. More generally, in the ceramic industry, the handling of fines is often problematic in pressing operations. The use of larger granulated precursors may resolve some of the deleterious effects of fines, providing their behaviour during compaction is well understood. Here, coupling DEM simulations and experimental characterizations, we have shown how internal defects or departure from monomodal size distribution affect the fracture behavior of porous microspheres that may act as granulated precursors. Although residual porosity is the best predictor for anticipating the approximate strength of a porous microsphere as described by the power law equation (2), defects that come inherently with industrial processing must be taken into account too for a full understanding of the fracture behavior of porous microspheres.

The force versus displacement curves that were obtained experimentally in [11] indicate a clear brittle behavior for the crushing of a microsphere between platens. This would suggest that tensile stresses are at play deep inside the microsphere as classically described when interpreting the crushing of spheres or the diametrical compression of cylinders (Brazilian test). The DEM simulations carried out in this work contradict this oversimplified view for the microspheres studied here. This is because the microsphere is made of aggregates that bond together. The particulate nature of the microsphere (instead of a fully dense and continuous material) implies that damage brought by the concentration of shear and compressive stresses drives the initiation of a macroscopic crack just under the contact.

This explains why the defects that expand closest to the surface of microspheres are the most detrimental for strength for a given volume fraction. It also calls for caution in categorizing this strength as tensile strength as it is mostly driven by shear and compressive stresses at the contact point. The stiff platens used here do not allow for a tensile strength to be measured for these very weak microspheres as discussed in [28]. Still, the DEM simulations carried out here provide a good approximation of microsphere-microsphere contacts as our periodic simulations demonstrate. These contacts and the gradual crushing of microspheres will dictate the behavior of the powder during close-die compaction.

Going beyond the idealized defects studied here (spherical or elliptic) was possible thanks to the coupling of DEM and of X-ray nanotomography. Provided the image resolution is sufficient, the defect can be accurately represented in DEM. The effect of such real defects can be properly anticipated with DEM simulations. Although representing less than 5 % of the total microsphere volume, the defect accounts for an approximately 30% drop in strength.

The next step consists in carrying DEM simulations with a sufficient number of microspheres to mimic a representative volume of powder during close-die compaction. As DEM is based on an explicit scheme, the discrete simulations conducted here on a single microsphere are already quite CPU intensive. Typically the CPU time necessary for the full crushing of a single microsphere is of the order of 12 days in sequential mode (or less than two days when

parallel computing is used with 8 cores). Thus, even though parallel computing is available with our in-house dp3D code, a cautious strategy is needed to calculate large scale close-die compaction problems with millions of particles.

Acknowledgements We would like to acknowledge the help of Pr. Luc Salvo from SIMaP laboratory for carrying out X-ray nanotomography experiments. The authors are also thankful to Emmanuelle Brackx and Renaud Domenger for their assistance during in-situ micro compression tests.

References

[1] D. Prieur, A. Jankowiak, C. Leorier, N. Herlet, L. Donnet, P. Dehaudt, C. Maillard, J.-P. Laval, P. Blanchart, Fabrication and characterization of minor actinides bearing fuels obtained by conventional powder metallurgy process, Powder technology 208 (2) (2011) 553–557.

[2] D. Prieur, A. Jankowiak, T. Delahaye, N. Herlet, P. Dehaudt, P. Blanchart, Fabrication and characterisation of {U}$_{0.85}${Am}$_{0.15}${O}$_{2-x}$ discs for MARIOS irradiation program, Journal of Nuclear Materials 414 (3) (2011) 503–507.

[3] G. W. Weber, R. L. Beatty, V. J. Tennery, Processing and Composition Control of Weak-Acid-Resin-Derived Fuel Microspheres, Nuclear Technology 35 (2) (1977) 217–226.

[4] S. M. Tiegs, P. A. Haas, Improved fuel pellet fabrication using gel microspheres, Transactions of the American Nuclear Society 33 (Nov) (1979) 273–275.

[5] E. Zimmer, C. Ganguly, J. Borchardt, H. Langen, {SGMP} an advanced method for fabrication of {UO}2 and {MO}x fuel pellets, Journal of Nuclear Materials 152 (2) (1988) 169–177.

[6] S. Picart, H. Mokhtari, I. Jobelin, Method for preparing a mixed fuel comprising uranium and at lesat one actinide and/or lanthanide applying a cation exchange resin, US Patent 9,330,795 B2.

[7] R. D. Hunt, J. L. Collins, M. H. Lloyd, S. C. Finkeldei, Production of more ideal uranium trioxide microspheres for the sol-gel microsphere pelletization process without the use of carbon, Journal of Nuclear Materials 515 (2019) 107–110. doi:10.1016/j.jnucmat.2018.12.029.
URL https://doi.org/10.1016/j.jnucmat.2018.12.029

[8] S. Picart, P. Parant, M. Caisso, E. Remy, H. Mokhtari, I. Jobelin, J. P. Bayle, C. L. Martin, P. Blanchart, A. Ayral, T. Delahaye, Porous metal oxide microspheres from ion exchange resin, The European Physical Journal Special Topics 224 (9) (2015) 1675–1687. doi:10.1140/epjst/e2015-02490-y.
URL https://hal.archives-ouvertes.fr/hal-01218308http://link.springer.com/10.1140/epjst/e2015-02490-y

[9] S. Picart, A. Gauthe, P. Parant, M. Caisso, E. Remy, I. Jobelin, J. M. Pomarede, P. Grangaud, M. Bataille, C. Frost, J. Dauby, J. P. Bayle, F. Delage, T. Delahaye, C. L. Martin, A. Ayral, The Weak Acid Resin Process: A Dustless Conversion Route for the Synthesis of Americium Bearing-blanket Precursors, Procedia Chemistry 21 (2016) 271–278.

[10] L. Ramond, P. Coste, S. Picart, A. Gauthé, M. Bataille, Fabrication of ({U},{A}m){O}2 pellet with controlled porosity from oxide microspheres, Journal of Nuclear Materials 492 (2017) 97–101.

[11] P. Parant, E. Remy, S. Picart, J. P. Bayle, E. Brackx, A. Ayral, T. Delahaye, C. L. Martin, Mechanical behaviour of porous lanthanide oxide microspheres : Experimental investigation and numerical simulations, Journal of the European Ceramic Society 38 (2) (2018) 695–703. doi:10.1016/j.jeurceramsoc.2017.09.024.
URL https://hal.archives-ouvertes.fr/hal-01678678http://dx.doi.org/10.1016/j.jeurceramsoc.2017.09.024

[12] A. D. Jefferson, I. C. Mihai, The simulation of crack opening–closing and aggregate interlock behaviour in finite element concrete models, International Journal for Numerical Methods in Engineering 104 (1) (2015) 48–78.

[13] Z. Tianshu, P. Hing, H. Huang, J. Kilner, Ionic conductivity in the CeO2–Gd2O3 system (0.05 Gd/Ce 0.4) prepared by oxalate coprecipitation, Solid State Ionics 148 (3-4) (2002) 567–573.

[14] V. Grover, A. K. Tyagi, Phase relations, lattice thermal expansion in {C}e{O}2{G}d2{O}3 system, and stabilization of cubic gadolinia, Materials Research Bulletin 39 (6) (2004) 859–866. doi:https://doi.org/10.1016/j.materresbull.2004.01.007.

[15] P. Parant, Compaction de microspheres poreuses d'oxyde de lanthanides : approches experimentale et simulations numeriques., Ph.D. thesis, Univ. Grenoble Alpes (2016).

[16] C. L. Martin, D. Bouvard, G. Delette, Discrete Element simulations of the Compaction of aggregated ceramic powders, J. Am. Ceram. Soc. 89 (2006) 3379–3387.

[17] A. Balakrishnan, P. Pizette, C. L. Martin, S. V. Joshi, B. P. Saha, Effect of particle size in aggregated and agglomerated ceramic powders, Acta Mater. 58 (2010) 802–812.

[18] P. Pizette, C. L. Martin, G. Delette, F. Sans, T. Geneves, Green strength of binder-free ceramics, J. Eur. Ceram. Soc. 33 (2013) 975–984. doi:10.1016/j.jeurceramsoc.2012.11.018.
URL www.sciencedirect.com

[19] G. Jefferson, G. K. Haritos, R. M. McMeeking, The elastic response of a cohesive aggregate - a discrete element model with coupled particle interaction, J. Mech. Phys. Solids 50 (2002) 2539–2575.

[20] D. Jauffrès, C. L. Martin, A. Lichtner, R. K. Bordia, Simulation of the elastic properties of porous ceramics with realistic microstructure, Modell. Simul. Mater. Sci. Eng. 20 (4) (2012) 45009. doi:10.1088/0965-0393/20/4/045009.

[21] D. O. Potyondy, P. A. Cundall, A bonded-particle model for rock, Int. J. Rock Mech. Min. Sci. 41 (8) (2004) 1329–1364. doi:10.1016/j.ijrmms.2004.09.011.

[22] X. Liu, C. L. Martin, D. Bouvard, S. Di Iorio, J. Laurencin, G. Delette, S. D. Iorio, J. Laurencin, G. Delette, Strength of Highly Porous Ceramic Electrodes, J. Am. Ceram. Soc. 94 (10) (2011) 3500–3508. doi:10.1111/j.1551-2916.2011.04669.x.

[23] E. Remy, Etude de la synthese de spheres d'oxyde d'actinides et/ou de lanthanides et de leur aptitude a la ceramisation., Ph.D. thesis, Universite de Montpellier II (2013).

[24] R. Ferreira, E. Jordão, A model for the behavior of thorium uranium mixed oxide kernels in the pelletizing process, Journal of Nuclear Materials 350 (3) (2006) 271–283. doi:10.1016/j.jnucmat.2005.12.006.
URL http://linkinghub.elsevier.com/retrieve/pii/S0022311506000535

[25] Y. Hiramatsu, Y. Oka, Determination of the tensile strength of rock by a compression test of an irregular test piece, International Journal of Rock Mechanics and Mining ... 3 (1966) 89 – 99.
URL http://www.sciencedirect.com/science/article/pii/0148906266900027

[26] K. T. Chau, X. X. Wei, R. H. Wong, T. X. Yu, Fragmentation of brittle spheres under static and dynamic compressions: Experiments and analyses, Mechanics of Materials 32 (9) (2000) 543–554. doi:10.1016/S0167-6636(00)00026-0.

[27] P. H. Shipway, I. M. Hutchings, Fracture of brittle spheres under compression and impact loading. I. Elastic stress distributions, Philosophical Magazine A 67 (6) (1993) 1389–1404. doi:10.1080/01418619308225362.

[28] V. Pejchal, G. Žagar, R. Charvet, C. Dénéréaz, A. Mortensen, Compression testing spherical particles for strength: Theory of the meridian crack test and implementation for microscopic fused quartz, Journal of the Mechanics and Physics of Solids 99 (July 2016) (2017) 70–92. doi:10.1016/j.jmps.2016.11.009.

[29] H. A. Carmona, F. K. Wittel, F. Kun, H. J. Herrmann, Fragmentation processes in impact of spheres, Physical Review E - Statistical, Nonlinear, and Soft Matter Physics 77 (5) (2008) 1–10. arXiv:0711.2993, doi:10.1103/PhysRevE.77.051302.